Measuring the Phase of Light

Matthew D. Lew
Xiquan Cui
Changhuei Yang
Department of Electrical Engineering
California Institute of Technology

"Sight is perhaps the most important of our five senses, allowing us to examine the universe around us from up close and afar. However, our eyesight fails us more often than we realize."

SIGHT IS PERHAPS THE MOST IMPORTANT of our five senses, allowing us to examine the universe around us from up close and afar. However, our eyesight fails us more often than we realize. Take for instance a bird that repeatedly plummets against a spotless window or a biologist who must stain a cell in order to examine its internal features with a microscope. Our eyes are useless when we wish to inspect the structure within transparent objects. Eyes, as well as cameras, ignore a critical characteristic of light – its phase.

Dr. Changhuei Yang and the students in his Biophotonics Laboratory at the California Institute of Technology work to conquer diagnostic and measurement problems in biomedicine. Many of the techniques they use involve characterizing and manipulating the phase of light.

THE NATURE OF LIGHT

Light can generally be described by three parameters: wavelength, amplitude, and phase. The human eye can discern the wavelength, or color, and amplitude, or brightness, of light with ease, but the picture painted by our eyes is incomplete. Our eyes cannot perceive the phase of light. Light is wavelike and periodic in nature; its amplitude varies like a sinusoid as it travels through space. The phase of light describes where the light is as it traces out this sinusoid. Our eyes average or blur this variation over time to allow us to see light's intensity, effectively throwing away the phase information. However there are situations in which a lot of information is encoded within the phase of light.

Microscopy is a particularly good example of an instance where phase is important. Figure 1 shows that differential interference contrast (DIC) microscopy can reveal features that are invisible in normal bright-field microscopy. DIC microscopy reveals variations in the gradient of, or change in, effective optical path length within a sample by using interference, hence the term differential interference contrast. The effective optical path length is proportional to the phase of light and is affected by the sample's index of refraction. Air has an index of refraction equal to 1, while glass has an index of refraction of 1.5. For light waves, traveling through one meter of glass is the same as traveling

through 1.5 meters of air; they each have the same effective optical path length. Since the index of refraction is a material property, many interesting features can be revealed by DIC microscopy.

However, traditional Nomarski DIC microscopy has major disadvantages: its differential phasecontrast images are qualitative, non-linear, and contain both amplitude and phase information. Quantitative phase contrast images are particularly useful in cell biology, with applications ranging from cell dynamics studies to disease pathology. In addition, traditional DIC cannot reliably image anisotropic samples, in which the index of refraction can depend on the polarization axis of the light. This is a major drawback in biological applications, since many organic samples are birefringent. Finally, traditional DIC requires expensive and fragile optical components, including several Wollaston prisms, quarter wave plates, and polarizers.

A NOVEL APPROACH

Our device utilizes the phenomena of interference and diffraction. Interference occurs when two or more beams of coherent light interact with one another; the waves sum together and can interfere constructively or destructively, producing bright and dark fringes. Coherent light refers to light whose rapid fluctuations in amplitude and phase are correlated; light emitted from a laser is an example of coherent light.

Diffraction refers to the bending or spreading of light as it propagates through space. This effect is most pronounced after light passes through an aperture whose size is comparable to its wavelength. The simplest example is the diffraction pattern from a small pinhole. Instead of a stream of particles emerging from the pinhole, light is more accurately pictured as a hemispherical pattern of wavefronts emanating from the pinhole.

We propose an innovative method for performing DIC microscopy that eliminates the aforementioned shortcomings of traditional DIC while being simple and easily integrable for on-chip microscopy. Our device utilizes a commercially available Micron complimentary metal oxide semiconductor (CMOS) grayscale image sensor. This sensor features pixels which are 10 µm x 10 µm in size and can serve as a foundation for microfabrication.

We spin-coat a 120 µm thick layer of SU-8, a photoresist which is transparent to visible light, on top of the CMOS sensor. Then, a 20 µm thick layer of aluminum is evaporated on top of the SU-8. Finally, a focused ion beam (FIB) is used to etch two circular holes 500 nm in diameter, with 1 µm center-to-center spacing, in the aluminum. We use a monochromatic light source, a He-Ne laser, to illuminate a sample whose transmitted light propagates through the two holes. The light from the two holes interferes with one another and illuminate our CMOS imager. If there is no phase difference between the light that propagates through the two holes, the resulting interference fringes will be centered directly beneath the holes. However, if there is a phase difference, the interference pattern will translate accordingly. In effect, this device compares the phase of the light propagating through one hole to the phase of the light propagating through the other. By finding the relationship between fringe location and phase differential, we can obtain differential phase information directly from the CMOS camera images.

There are several techniques for building phase images from our differential phase portraits. The most obvious is line integration; each differential phase image can simply be integrated along the phase differentiating direction, or the axis connecting the holes. However, the resulting images will suffer from banding artifacts since the integration constant, which is generally different for each line integral, is thrown away during the differentiating operation performed by the holes. In addition, small phase errors associated with each pixel will accumulate as the line integration proceeds, thereby progressively degrading the image quality.

Another technique becomes apparent when we rewrite $\Delta\phi(x,y)$, the differential phase at location (x,y), as a convolution of two functions using the sifting property of Dirac delta functions:

$$\begin{aligned}\Delta\phi(x,y) &= \phi(x-\frac{1}{2}\Delta x, y-\frac{1}{2}\Delta y)-\phi(x+\frac{1}{2}\Delta x, y+\frac{1}{2}\Delta y)\\ &= g(x,y)\otimes\phi(x,y)\end{aligned} \quad (1)$$

where

$$g(x,y)=\delta(x-\frac{1}{2}\Delta x, y-\frac{1}{2}\Delta y)-\delta(x+\frac{1}{2}\Delta x, y+\frac{1}{2}\Delta y) \quad (2)$$

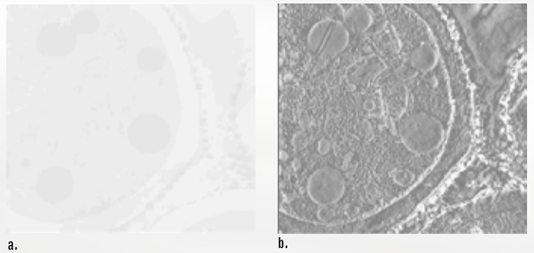

a.

b.

FIGURE 1

a. Bright-field image of an unstained liverwort spore, b. DIC picture of the same spore

These images reproduced from P. J. McMahon, E. D. Barone-Nugent, B. E. Allman, K. A. Nugent: "Quantitative phase-amplitude microscopy II: differential interference contrast imaging for biological TEM"

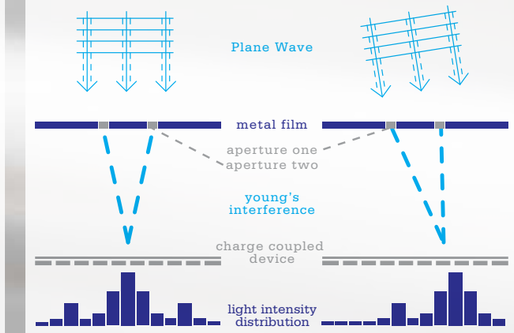

FIGURE 2

Geometry and overall operating principle of our device

$\phi(x,y)$ is the phase at location (x,y), Δx is the separation between the holes in the x-direction, and Δy is the separation between the holes in the y-direction. We can then isolate the phase by performing a deconvolution on (1) and dividing by $g(x,y)$. This process, however, is extremely noise-sensitive and requires the use of a Weiner filter in order to compensate. The optimal choice of filter parameters is subjective and requires the knowledge of the spectral distribution of the signal-to-noise ratio. As a result, reliably constructing quantitative phase information is difficult. A third method involves using the two-dimensional Hilbert transform. This method's primary weakness, however, is that it is not quantitatively accurate and therefore not useful for our application.

SIMULATIONS OF OUR DEVICE

Rigorously simulating the phase responsivity of this device requires us to numerically solve Maxwell's equations for our three-dimensional geometry, a task which is extraordinarily computationally expensive. However, by utilizing the Fraunhofer (far-field) approximation, we can greatly simplify the diffraction simulations. Consider the case where monochromatic light is incident upon an aperture, where

$$p(x,y)=\begin{cases}\exp(i\phi), & \textit{inside the aperture}\\ 0, & \textit{outside the aperture}\end{cases} \quad (3)$$

is the aperture function and ϕ represents the phase of the light propagating through the aperture. The diffraction pattern seen on

$$I(x,y)=\frac{I_i}{(\lambda d)^2}\left|P(\frac{x}{\lambda d},\frac{y}{\lambda d})\right|^2 \quad (4)$$

a viewing screen is just the Fourier transform of the aperture function where

$$P(\upsilon_x,\upsilon_y)=\int_{-\infty}^{\infty}\int_{-\infty}^{\infty}p(x,y)\exp\left[i2\pi(\upsilon_x x+\upsilon_y y)\right]dx\,dy \quad (5)$$

I, is the intensity of the incident light, λ is the wavelength of the incident light, and d is the distance between the aperture and the viewing screen. The validity of this approximation is assured by the "antenna designer's formula," which states that

$$d > \frac{2D^2}{\lambda} \quad (6)$$

where D is the linear dimension of the aperture. For our device, d is 1.5 µm and λ is 632.8 nm for our He-Ne laser, which implies that must be greater than 7.11 µm in order for the Fraunhofer approximation to hold. Since our CMOS imager is 120 µm below our holes, we satisfy this condition with two orders of magnitude to spare.

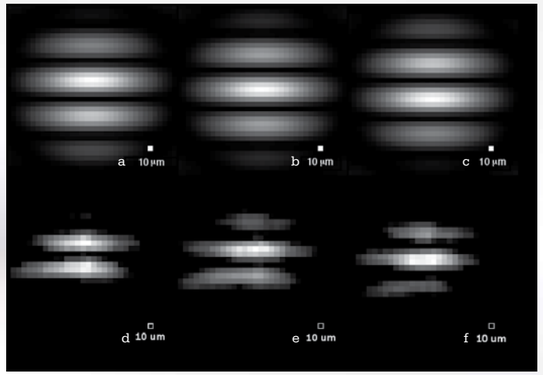

FIGURE 4

a) Simulated fringes produced by a -90° phase differential, b) simulated fringes produced by a 0° phase differential, c) simulated fringes produced by a 90° phase differential, d) measured fringes produced by a -90° phase differential as imaged with our device, e) fringes produced by a 0° phase differential, f) fringes produced by a 90° phase differential; device parameters are an illumination wavelength of 632.8 nm, two 500 nm diameter holes with 1 µm center-to-center spacing, 120 µm distance between holes and CCD pixels, and 10 µm x 10 µm CCD pixels

Using MATLAB, we modeled our aperture as a two-dimensional matrix and performed a fast Fourier transform (FFT) on it to find the diffraction pattern. We found that the diffraction pattern comprises three interference fringes. Furthermore, the simulations proved that these fringes shift as a function of the phase differential. This analysis was achieved quantitatively by using the curve-fitting tool within MATLAB to fit the zero-order, or center, fringe to a Gaussian curve, yielding a center location for that fringe. Mapping the fringe locations to their corresponding phase differentials produced a linear relationship across a 180 degree range of phase differentials.

Further simulation showed that larger holes create brighter fringes, and holes that are closer together produce larger fringes. These trends suggest that we should use the largest holes with the closest spacing, but there are fundamental physical limits. First, larger holes lower our spatial resolution, since we are comparing the phase between two circular sources of light instead of two point sources of light. Second, the two holes will couple light between one another when their spacing goes below a certain distance; instead of two small holes, we effectively have one large hole. This occurs because there is not enough metal between the two holes to attenuate the electromagnetic waves traveling between the two holes.

INITIAL IMAGES

Upon fabrication completion, our first task was to measure the phase responsivity of our device. We directed a collimated He-Ne laser beam onto our holes and mounted our device on a rotating stage, ensuring that the rotation direction of the stage was parallel to the axis connecting the two holes. Since the center-to-center spacing of the holes was much smaller than the laser beam width (1 µm versus 1 mm), we approximated the incident beam as a plane wave. If the laser beam is normal to our holes, there is no path length difference, and therefore no phase difference, between the light propagating through the two holes. We therefore controlled the phase difference between the two holes by rotating our device. A responsivity curve was created by mapping how phase differential corresponds to fringe location.

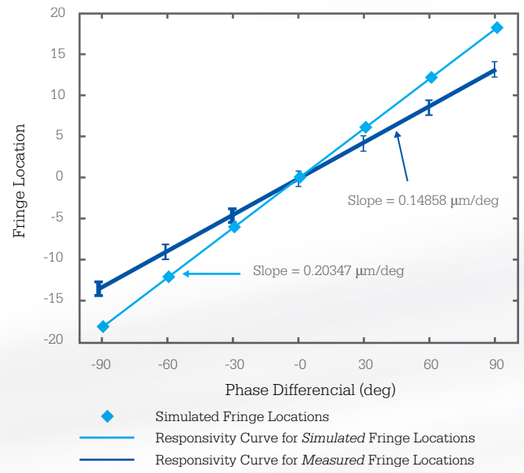

FIGURE 5
Simulated versus measured responsivity curves. Error bars represent the variation in measured fringe location at each phase differential.

The slope of the measured responsivity curve deviates from the theoretical curve by 25 percent. This is most likely due to the assumptions made in our simulations. By employing the Fraunhofer approximation, we implicitly assumed that scalar diffraction theory applies to our device. However, our aperture size is on the order of the light's wavelength. As such, the interaction of light at the dielectric interface between aluminum and air is significant. These coupling effects are ignored in our scalar diffraction model. Thus, accurate, quantitative simulations require numerically solving Maxwell's equations for our geometry.

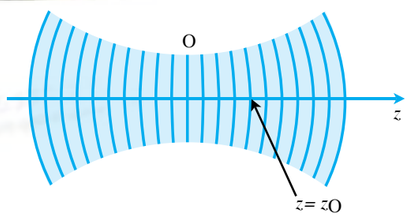

FIGURE 6
Wavefronts and regions of a Gaussian beam. The wavefronts are approximately planar near the waist and spherical far from the waist.

We then scanned a well-known phase profile to test our device. A Gaussian beam was chosen for its familiar behavior and because it can be generated and modified easily. Laser beams are Gaussian in nature, and Gaussian beams propagating through circularly symmetric optical components, such as lenses, remain Gaussian. The intensity of a Gaussian beam propagating in the z-direction is given by

$$I(x,y,z) = \frac{2P}{\pi W^2(z)} \exp\left[-\frac{2(x^2+y^2)}{W^2(z)}\right] \quad (7)$$

where

$$W(z) = W_0\left[1+\left(\frac{z}{z_0}\right)^2\right]^{\frac{1}{2}} \quad (8)$$

P is the beam's power, W_0 is its minimum waist size, and Z_0 is the Rayleigh range of the beam. $W(z)$ characterizes the expansion of the beam's cross-section as the beam propagates, and larger Rayleigh range values lead to slower beam expansion. As (7) shows, Gaussian beams are radially symmetric in the transverse or xy plane. Gaussian beams have three regions of interest for phase profiling: a converging section, the waist, and a diverging section [Figure 6]. The beam's phase profile is steepest far away from the beam waist and becomes progressively flatter towards the beam waist. We expect the phase portraits of the Gaussian beam to be bell-shaped, oriented upwards or downwards depending upon whether the beam is converging or diverging. The differential phase profiles should exhibit a zero degree phase differential near the center of the beam and be monotonic in the differentiating direction.

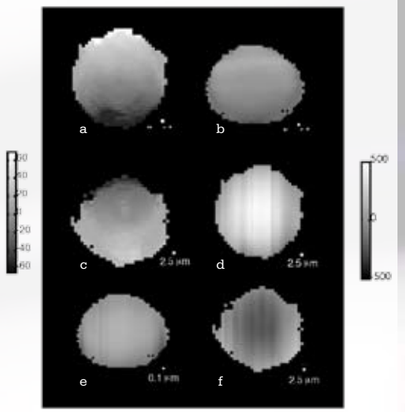

FIGURE 7
a) Differential phase profile of a converging Gaussian beam, b) differential phase profile of a beam's waist, c) differential phase profile of a diverging beam, d) reconstructed phase profile of a converging Gaussian beam, e) phase profile of a beam's waist, f) phase profile of a diverging beam; all color bars are in units of degrees

We imaged a Gaussian beam at each of its three sections to show the different phase and differential phase behavior associated with each section. The line integration method was used to construct phase profiles from the differential phase images, and vertical banding results since the axis connecting the holes, and thus the integrating direction, is vertical. Note the contrasting differential phase profiles between converging and diverging Gaussian beams, as well as the relatively flat profile of the beam's waist. In addition, the circularly symmetric phase profiles of the Gaussian beams are worth noting.

FUTURE DIRECTIONS

The major disadvantage of our current device is that it only differentiates phase in a single direction, making a full reconstruction of a sample's phase profile impossible. We have numerically simulated the behavior of a couple of geometries that would enable us to gather two-dimensional differential phase data. We plan to test these geometries in the lab in the near future.

We also plan to begin applying the technique and evaluating its performance for different applications. Besides the obvious biological applications, our technique is well suited for singular optics studies. Singular optics studies optical phenomena which contain one or more phase singularities, or areas where phase is undefined. These wavefronts have unusual phase behavior, and our device is well-suited to study them.

Optical vortices are prevalent in the world of singular optics. They can be described by the envelope function

$$u(\rho,\phi,z) = A_m(\rho,z)\exp(-im\phi)\exp[i\varphi_m(\rho,z)]$$

in cylindrical coordinates where the phase components are separable into a portion dependent on ϕ and a portion dependent upon p and z. m is the topological charge and is always an integer to satisfy phase continuity. The $exp(-im\phi)$ term is the most important, giving the optical vortex its characteristic helical wavefront. In any cross-section of an optical vortex where z is constant, phase is proportional to polar angle.

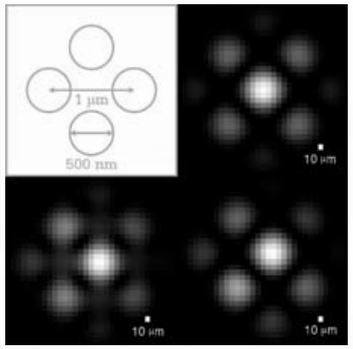

FIGURE 8
a) geometry for imaging 2D differential phase using 4 holes, b) simulated fringes from the 4 hole device with a 0° phase differential in both directions, c) fringes from the 4 hole device with a 90° phase differential in the horizontal direction, d) fringes from the 4 hole device with a 90° phase differential in both directions; simulation parameters are an illumination wavelength of 632.8 nm, 120 µm distance between holes and CCD pixels, and 10 µm x 10 µm CCD pixels

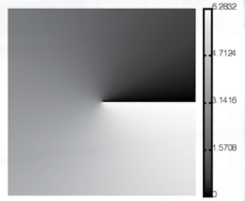

FIGURE 9
Phase profile of an optical vortex with a topological charge of 1.There is a phase singularity, and a corresponding point with zero intensity, at the center of the vortex.

There are many methods for generating optical vortices including spiral phase plates, fractal zone plates, or interfering three plane waves. However, the most practical methods utilize spatial light modulators (SLMs), computer-generated holograms (CGHs), or a combination of the two. We have computed the CGHs required to generate optical vortices of various topological charges. An advantage of employing our device to profile optical vortices is its ease of use. Conventional techniques for verifying the existence of optical vortices require interfering them with a plane wave and observing the resulting interference pattern. Our device would eliminate this tedious process and allow the quality of the optical vortex to be examined directly. We plan to perform differential phase imaging of these structures in the near future.

Although there is a significant error associated with utilizing scalar diffraction theory to predict the phase sensitivity of our device, we found that our device provides quantitative DIC images with high spatial resolution and phase sensitivity. Differential phase images of a Gaussian beam were captured with our device, enabling the partial construction of the beam's phase profile. Our technique has the advantages of being compact, low cost, and easily adaptable for on-chip microscopy. Furthermore, we can study diverse samples using our device, such as biological structures and optical vortices. □

ACKNOWLEDGEMENTS

I thank Professor Changhuei Yang and Xiquan Cui for their mentorship throughout this Summer Undergraduate Research Fellowship. I also appreciate the timely advice of Xin Heng, Jigang Wu, and Zahid Yaqoob as I endured the trials and tribulations that are the research process. I extend my gratitude to Mr. and Mrs. Anthony Skjellum for funding a considerable portion of my project. It is the donations of generous alumni like these that keep the Summer Undergraduate Research Fellowship alive at Caltech.

FURTHER READING

1. E. D. Barone-Nugent, A. Barty, and K. A. Nugent, "Quantitative phase-amplitude microscopy I: optical microscopy," Journal of Microscopy-Oxford 206, 194-203 (2002).

2. P. J. McMahon, E. D. Barone-Nugent, B. E. Allman et al., "Quantitative phase-amplitude microscopy II: differential interference contrast imaging for biological TEM," Journal of Microscopy-Oxford 206, 204-208 (2002).

3. M. R. Arnison, K. G. Larkin, C. J. R. Sheppard et al., "Linear phase imaging using differential interference contrast microscopy," Journal of Microscopy-Oxford 214, 7-12 (2004).

4. Bahaa E. A. Saleh and Malvin Carl Teich, Fundamentals of Photonics. (John Wiley & Sons, Inc., New York, 1991).

5. Joseph W. Goodman, Introduction to Fourier Optics, 3rd ed. (Roberts & Company Publishers, Englewood, 2005).

6. Z. S. Sacks, D. Rozas, and G. A. Swartzlander, "Holographic formation of optical-vortex filaments," Journal of the Optical Society of America B-Optical Physics 15 (8), 2226-2234 (1998).